RESEARCH ARTICLE - SOLID EARTH SCIENCES

Numerical modelling of the near-field velocity pulse-like ground motions of the Northridge earthquake

Quanbo Luo[1] · Feng Dai[1] · Yi Liu[1] · Mengtan Gao[2]

Abstract

The seismic records acquired during the 1994 M_W6.7 Northridge earthquake provide important data for studying the pulse-like ground motions in the vicinity of reverse faults. We selected 106 horizontal records from 468 strong ground motion records in the near-field region and rotated the original records into fault-parallel and fault-normal orientations. Large velocity pulses were simulated by the 3D finite difference method using a kinematic source model and a velocity structure model. Regression analysis was performed on the simulated and observed amplitudes of the velocity time history and response spectrum using the least-squares method. Our results show that the released energy and rupture time of asperities in the source model have important effects on the near-field velocity pulses, and the asperity near the initial rupture contributes more to the velocity pulses than does the asperity near the central region. The unidirectional and bidirectional characteristics of large velocity pulses are related to the thrust slip and rupture direction of the fault. The pulse period and the characteristic period are positively correlated with the rise time, and the pulse peak is regulated by multiple parameters of the subfaults. The distributions of the simulated PGV and Arias intensity agree well with the observed records, in which the contours exhibit asymmetric distribution and irregular elliptical attenuation in the near-field region, and the distributions exhibit a significant directivity along the fault. Moreover, the attenuation rate decreases with increasing distance from the fault. In addition, the fault-normal component is larger than that on the fault-parallel component, and the former decays faster. Velocity pulses larger than 30 cm/s are most likely to be distributed within approximately 15 km from the fault plane of the Northridge earthquake. Thus, the revealed pattern of the near-field velocity pulse-like ground motions indicates their close relation with the most severe earthquake effects.

Keywords Northridge earthquake · Finite difference method · Large velocity pulse · Source model · PGV · Response spectrum · Arias intensity

Introduction

On 17 January 1994, at 4:31 local time (12:31 UTC), an earthquake of magnitude M_W6.7 took place in the Northridge area northwest of Los Angeles, California. The epicentre was located in San Fernando Canyon at (34.206° N, 118.554° E) with a shallow focal depth of approximately 17.5 km, as shown in Fig. 1. This strong earthquake caused many casualties and property losses, leading to more than 60 deaths and 9000 injuries, and a large number of high-rise buildings and bridges were damaged (Liu et al. 2012). The Northridge area is located on the West Coast of the USA within the largest seismic belt in the world, namely the circum-Pacific Ring of Fire, which displays a high incidence of earthquakes.

When a causative fault ruptures with a velocity close to the shear wave, the earthquake rapidly releases the enormous strain energy accumulated during the long-term tectonic movement. The large velocity pulses are characterized by high amplitude, long period, which arrive early at time histories as simple harmonic oscillations. Based on their characteristics, velocity pulses are divided into one-side and two-side pulses (Kawase and Aki 1990; Heaton et al. 1995; Oglesby and Archuleta 1997). These large velocity pulses

✉ Yi Liu
liuyi_scu@163.com

1 State Key Laboratory of Hydraulics and Mountain River Engineering, College of Water Resource and Hydropower, Sichuan University, Chengdu, Sichuan 610065, China

2 Institute of Geophysics, China Earthquake Administration, Beijing 100081, China

Fig. 1 A topographic map of the Northridge area. The dashed rectangle depicts the surface projection of the causative fault plane for the Northridge earthquake. The strong ground motion stations are indicated by triangles, and stations with and without pulse records are indicated by red triangles and black triangles, respectively. The surrounding cities of the Northridge earthquake are marked with the blue open circles. The epicentre is marked with a star
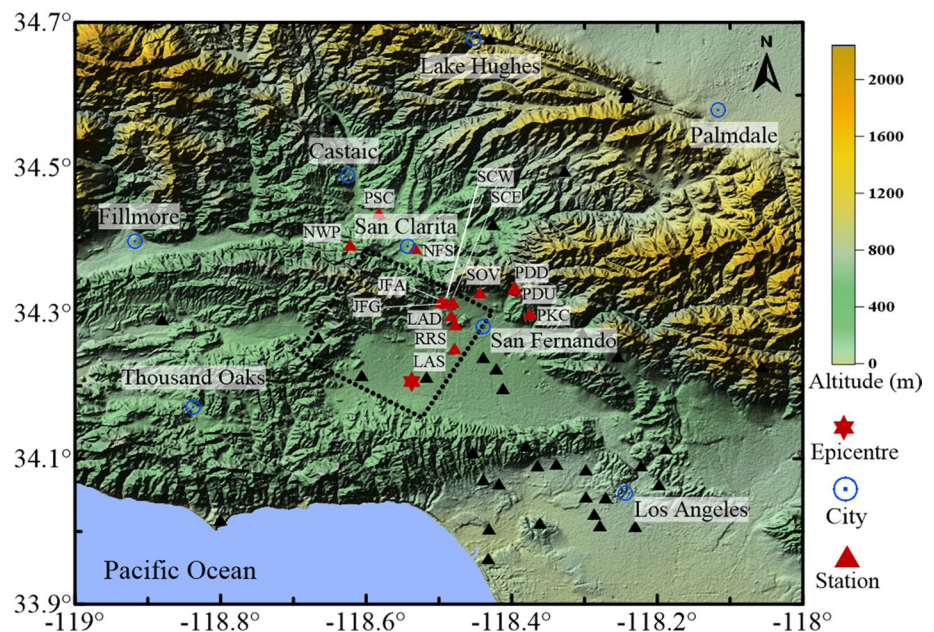
can cause substantial damage to large structures, as they can easily cause large inter-story displacements and permanent deformation (Bertero et al. 1978; Malhotra 1999; Li et al. 2020). In recent years, a small number of velocity pulses have been recorded during global earthquakes; for example, 29 pulses were recorded in the 1999 M_W7.6 Chi–Chi earthquake, 9 in the 2010 M_W7.0 Darfield earthquake, and 7 in the 2008 M_W7.9 Wenchuan earthquake. These earthquakes have attracted considerable interest in the fields of seismology and engineering. With the rapid development of the technology, buildings with higher natural vibration periods (large bridges, high-rise buildings, and oil storage tanks) are gradually proliferating. Therefore, the study of near-field long-period velocity pulses is of great significance for seismic hazard analysis and seismic design.

Because of the uncertainties in ground motions and the scarcity of seismographs, the Pacific Earthquake Engineering Research Center (PEER) has collected fewer than 200 pulse recordings, which is a rather poor sample to provide a statistical model of the characteristics of pulse-like ground motions. In order to compensate for the shortage of pulse records, models that can effectively simulate velocity pulses have been proposed by several researchers (Dickinson and Gavin 2011; Li 2016; Pu et al. 2017). However, models based on engineering approaches do not account for the rupture history. To cope with this, deterministic methods have been proposed to simulate the near-field velocity pulses emitted from large seismogenic sources.

For the simulation of time histories within the low period range of engineering interest (< 1 s), the stochastic (Boore 2003; Motazedian and Atkinson 2005; Zhang and Yu 2010) and empirical Green's function (Irikura

1983; Choudhury et al. 2016) methods are usually used. Beresnev and Atkinson (1998a) performed a successful simulation of the acceleration histories that recorded the 1985 M_W 8.1 Mexico earthquake by using the stochastic finite-fault method. Li et al. (2017) simulated the acceleration records of the 1997 Kyushu earthquake by using the empirical Green's function method and analysed the relevant engineering parameters. The above methods are widely used for simulating short-period strong ground motions, but the simulation accuracy of near-field long-period ground motions is low (Irikura 1983; Li et al. 2018). Alternatively, for the low-frequency components (less than 1 Hz) in near-field ground motions, it is more suitable to apply a deterministic method.

Long-period ground motions can be effectively simulated by the 3D finite difference method (Kramer 1996; Graves 1998; Pitarka 1999; Luo et al. 2019). Many seismologists have verified the feasibility of the 3D finite difference method for simulating the near-field long-period ground motions of different earthquakes, the research results of which provide important guidance for disaster reduction. Gao et al. (2002) simulated the basin effect in Beijing and noted that the amplification factor of the local area is approximately 2. Maeda et al. (2016) performed a seismic hazard analysis of long-period ground motions generated by many scenarios of a megathrust earthquake in Nankai. Furumura et al. (2019) simulated the propagation of seismic waves in heterogeneous structures and forecasted the long-period ground motions generated by large earthquakes in sedimentary basins, and validated the effectiveness of the finite difference method by using observed waveform data from the 2007 M_W6.6 Niigata and 2011 M_W9.0 Tohoku earthquakes.

This study attempts to simulate the near-field large velocity pulses of the 1994 Northridge earthquake using the 3D finite difference method. This paper is organized as follows. Firstly, we describe the simulation method and the source function. Then, the near-field velocity pulses are identified from the seismic records of the Northridge earthquake. "Model and parameter setting" section establishes the kinematic source model and velocity structure model and presents the regional calculation parameters. In "Results and discussion" section, the characteristics and distribution fields of the near-field velocity pulse-like ground motions are illustrated through the comprehensive analysis and discussion of the numerical simulation results. The results can reveal the causes of large velocity pulses and help to analyse the responses of large-scale engineering structures to ground motions. "Conclusions" section summarizes the whole study.

Finite difference simulation method

Compared with the finite element method and the discrete wavenumber method, the finite difference method proposed by Aki (1968) can effectively simulate long-period ground motions in a large area consisting of an inhomogeneous medium. In the finite difference method, which has been continuously improved by seismologists over the decades (Mikumo et al. 1987; Aoi and Fujiwara 1999), the study area can be divided into discrete grids in the horizontal and vertical directions based on the different characteristics of geological structures, which greatly improves the calculation efficiency while ensuring the calculation accuracy. The relationship between the velocity pulses and the source model parameters in the near-field long-period ground motions can be studied utilizing the 3D finite difference method.

To simulate the long-period velocity pulses with the 3D finite difference method, it is necessary to establish a suitable source model including the geometric parameters and kinematic parameters. The fault plane is divided into finite discrete grids, and then the slip, seismic moment, and source time function are embedded into the velocity–stress difference equation to obtain the velocity history generated during the earthquake (Aoi et al. 2012; Maeda et al. 2014; Iwaki et al. 2016). The source function is the temporal and spatial function of each subfault during the rupture process. We use the Ricker wavelet to simulate the near-field long-period velocity pulses generated by the Northridge earthquake:

$$g(t) = (1 - 2\pi^2 f_c^2 t^2) \exp(-\pi^2 f_c^2 t^2) \tag{1}$$

where $g(t)$ is the amplitude of the Ricker wavelet and f_c is the characteristic frequency, i.e. the reciprocal of the rise time of the subfault from initial rupture to slip termination. Figure 2 shows waveforms with characteristic frequencies
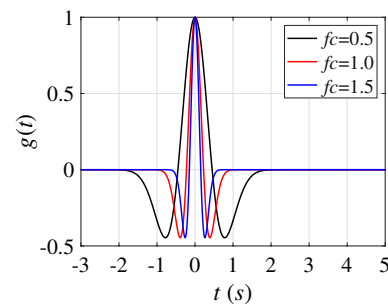

Fig. 2 The waveforms corresponding to the source function with characteristic frequencies of 0.5, 1, and 1.5 Hz

of 0.5, 1, and 1.5 Hz. The wavelet function proposed by Ricker (1943) is widely used to simulate seismic waves (Ji et al. 2002; Wang 2015; Liu et al. 2016). The seismic wave received by a station on the surface is usually a short vibration that is excited by the subfault and propagates through the underlying medium.

Strong motion recordings

The Next Generation Attenuation (NGA) database includes a large number of strong motion records from the Northridge earthquake, providing valuable fundamental data for studying near-field large velocity pulses. However, few stations are situated near the fault, and the spacing is variable; thus, a relatively small number of velocity pulses were recorded during this earthquake. Baker (2007) proposed three criteria for identifying velocity pulses: The pulse index in formula (2) is greater than 0.85, and the pulse appears early in the velocity time history and the peak ground velocity (PGV) is greater than 30 cm/s.

$$PI = 1/[1 + e^{-23.3 + 14.6(PGV_{ratio}) + 20.5(E_{ratio})}] > 0.85 \tag{2}$$

where PI is the pulse index, PGV_{ratio} is the ratio of the residual PGV to the original record after the velocity pulse is extracted, E_{ratio} is the ratio of the residual energy to the original record.

We selected 106 horizontal records in the study area from 468 strong motion records and identified 14 stations with velocity pulses and 39 stations without pulses based on the above criteria. For the stations that recorded velocity pulses during the Northridge earthquake, PKC and NWP are located at the ends of the fault, and 7 stations (LAS, RRS, LAD, SCE, SCW, JFA, and JFG) are located on the hanging wall, while the remaining stations are located on the footwall; the pulse data from these stations are listed in Table 1. Because the velocity waveforms recorded in the vertical direction do not meet the pulse standard and buildings

Table 1 Basic information of the 14 stations that recorded velocity pulses

Abbrev.	Station Name	Lat. (°N)	Long. (°W)	PGV-FP (cm/s)	PGV-FN (cm/s)	ClstD (km)	Owner
PKC	Pacoima Kagel Canyon	34.296	118.375	29.5	56.3	7.26	CDMG
PDU	Pacoima Dam Upper Left	34.330	118.396	22.9	67.8	7.01	CDMG
PDD	Pacoima Dam Downstream	34.334	118.396	12.5	47.9	7.01	CDMG
LAS	LA-Sepulveda VA Hospital	34.249	118.479	48.1	47.1	8.44	USGS
SOV	Sylmar-Olive View Med FF	34.326	118.444	43.3	102.8	5.30	CDMG
RRS	Rinaldi Receiving Station	34.281	118.478	46.2	117.4	6.50	LADWP
LAD	LA Dam	34.294	118.483	51.5	74.7	5.92	LADWP
SCE	Sylmar-Converting Station East	34.312	118.481	66.3	90.5	5.19	LADWP
SCW	Sylmar-Converting Station West	34.311	118.490	81.5	121.0	5.35	LADWP
JFA	Jensen Filter Plant Administrative Bld.	34.312	118.496	90.9	104.3	5.43	USGS
JFG	Jensen Filter Plant Generator Bld.	34.313	118.498	58.2	69.3	5.43	USGS
NFS	Newhall-Fire Station	34.387	118.533	33.6	84.6	5.92	CDMG
PSC	Pardee-SCE	34.435	118.582	72.4	50.7	7.46	SCE
NWP	Newhall-W. Pico Canyon Rd.	34.391	118.622	69.0	108.4	5.48	USC

ClstD is the closest distance from the recording station to the ruptured area. Owner is the name of agency that collected the data

USGS U.S. Geological Survey, *LADWP* Los Angeles Department of Water and Power, *CDMG* California Division of Mines and Geology, *USC* University of Southern California, *SCE* Southern California Edison

are affected mainly by horizontal vibrations, this paper studies only the horizontal components of the near-field ground motions. Considering that the directivity effect and the source radiation have different influences on the horizontal components, to obtain a reference for a seismic comparison and to establish a relationship between the original seismic records and the strike of the fault, we rotate the original orthogonal horizontal components into fault-parallel (N122° E) and fault-normal (N212° E) orientations.

Model and parameter setting

Source model

The focal depths determined by the CMT Project, PEER, and USGS range from 16.8 to 18.2 km (with an average of approximately 17.5 km); the strike is S58° E, and the dip angle of the fault plane is approximately 40° to the southwest. To clarify the fault geometry and rupture motion characteristics of the Northridge earthquake, numerous scholars have performed considerable research. Zeng and Anderson (1996) obtained a composite source model of the earthquake using a genetic algorithm and indicated that a large amount of slip occurred near the central source region. Wald et al. (1996) combined teleseismic, strong motion, GPS displacement, and permanent uplift recordings to obtain the slip distribution characteristics of the Northridge earthquake. Beresnev and Atkinson (1998b) divided the fault plane into 20 subfaults and verified the slip distribution characteristics on the fault plane by using the simulated acceleration

histories at 28 rock sites. The above results show that the fault geometry can be represented by a rectangular plane with a complicated and inhomogeneous distribution of slip.

The Northridge earthquake was triggered by a blind causative fault (Wald et al. 1996; Ji et al. 2002). The rupture occurred along a thrust from approximately 20 km to 5 km below the surface at a dip angle of 40° and was truncated by the San Fernando fault (Mori et al. 1995). We have established a source model formed by a rectangular plane in this study (Fig. 3). The fault ruptured 18 km along the strike approximately 5 km below the surface and ruptured
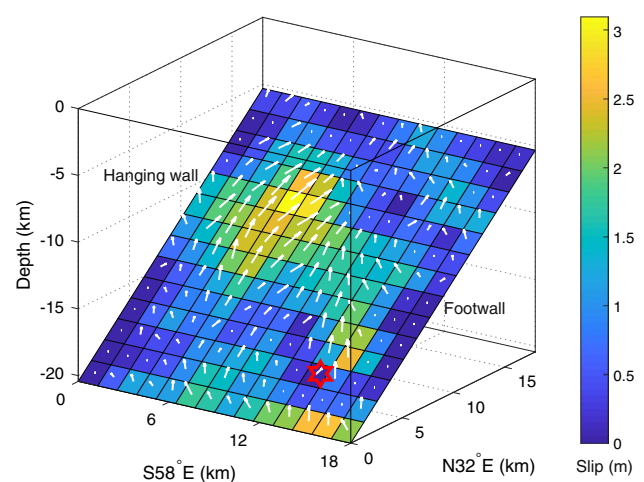
Fig. 3 The fault model of the Northridge earthquake. The fault plane is divided into 196 subfaults, each showing the direction of the average slip with an arrow and the magnitude of the average slip with colour. The hypocentre is indicated by a star

downward approximately 24 km along dip. The projection of the fault plane on the surface forms the black dashed rectangle shown in Fig. 1. We divided the entire fault plane into 196 subfaults of 1.286×1.714 km.

The energy generated by the rupture of an asperity during an earthquake greatly contributes to the strong ground motion; thus, the source model of an asperity is significant for evaluating the seismic effect on an engineering structure (Kamae and Irikura 1998). The strength of the asperity region is less than the stress field, thereby enhancing the fault rupture, which experiences a high stress drop during the rupture of the fault (Aki 1984). We extracted the position, quantity, and area of the asperities from the inhomogeneous slip distribution and assumed two asperities for the Northridge earthquake (Fig. 4): small asperity A is approximately 19.8 km², and large asperity B is approximately 72.7 km². Somerville et al. (1999) studied the spatial slip distribution of 15 crustal earthquakes with magnitudes greater than 5.7 worldwide and proposed that the area ratio of asperities to the entire fault is 0.22, and Murotani et al. (2008) proposed that the area ratio of a plate boundary earthquake is close to 0.2. In this study, the ratio of the total area of both asperities to the area of the entire fault is approximately 0.21, which is basically consistent with Somerville et al. (1999). In previous studies, i.e. the 1997 M_W6.0 Kagoshima, 2000 M_W6.6 Tottori, and 2004 M_W6.6 Chuetsu earthquakes (Irikura and Miyake 2011; Iwaki et al. 2016), asperities have been

approximated by a rectangle. However, the large slip on the fault plane is not necessarily located in a rectangular area. Based on the spatial inhomogeneity of the slip distribution (Wald et al. 1996), we set asperities A and B of the Northridge earthquake to have rectangular and irregular shapes, respectively.

The seismic moment is used to measure the energy released by an earthquake and thus has an important influence on the ground motion. The distribution of the seismic moment on the fault plane is shown in Fig. 4. This study determined that the total seismic moment of the Northridge earthquake is 1.15×10^{19} N m, which is close to $1.3 \pm 0.2 \times 10^{19}$ N m estimated by Wald et al. (1996). The seismic moment of the asperities and background region are distributed according to formula (3) proposed by Somerville et al. (1999), where the total seismic moment of both asperities is approximately 7.47×10^{18} N m, and that of the background region is 4.03×10^{18} N m.

$$M_{oa} = \mu D_a S_a \tag{3}$$

where μ is the average crustal rigidity, its value is about 30 Gpa. M_{oa} is the seismic moment of the asperity, and S_a is the area of the asperity. D_a is the average slip of the asperity, and its value (approximately 2.7 m) is the total slip on the asperity divided by the number of subfaults.

In our model, the Northridge earthquake began with a circular rupture near the bottom of the fault plane that propagated from the southeast to the northwest with an average rupture velocity of 2.8 km/s. Field et al. (1998) studied the nonlinear sediment response during the Northridge earthquake using a uniform circular rupture pattern, and the results indicated the effectiveness of circular rupture. Hartzell et al. (1996) found that the fault rupture velocity at the early stage of the earthquake was 2.8–3.0 km/s, while the velocity after 3 s was 2.0–2.5 km/s. We used a varying rupture velocity for the source rupture pattern: the velocity rapidly decreased outward from 3.0 km/s in the nucleation zone to 2.5 km/s over a total rupture time of approximately 8 s. The rise time of the fault slip is inhomogeneously distributed (Hartzell et al. 1996; Wald et al. 1996), and the nucleation zone is relatively small at approximately 0.6 s, although the rise time tends to increase outward, as shown in Fig. 5.

Velocity structure model

The crustal velocity structure reflects the stratigraphic sequence from the surface to the Moho and the variation in the seismic velocity with depth. A reasonable velocity structure model, which has an important influence on the simulation results of long-period velocity pulses, can be established according to the changes in the physical properties of each layer. In the numerical simulation of near-field
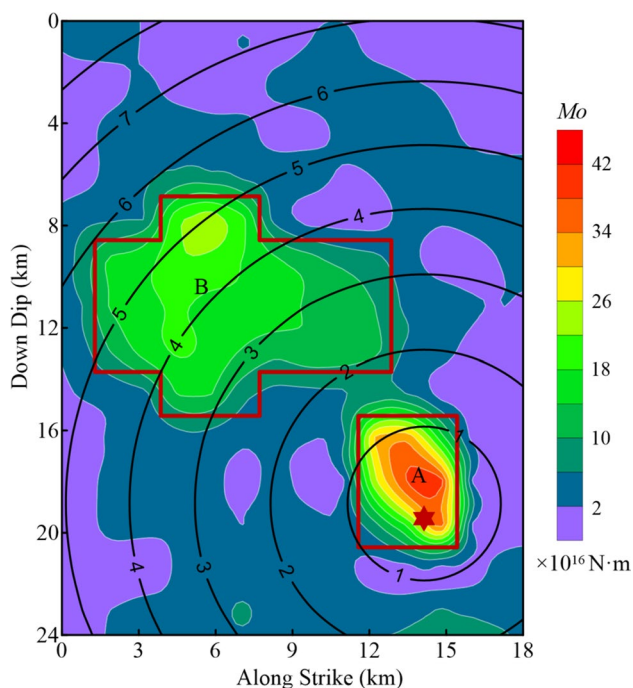

Fig. 4 The seismic moment distribution of the Northridge earthquake. The asperities are surrounded by red lines. The black lines are contours of rupture time at 1 s intervals
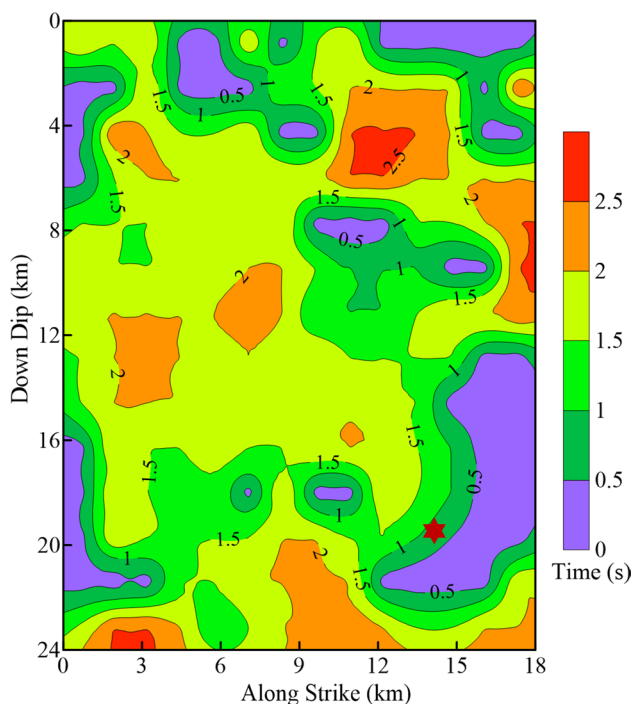
Fig. 5 The rise time distribution of the fault displacement; the adjacent contours are separated by 0.5 s intervals

same time, we used a non-uniform grid to divide the study region (Fig. 6). In the upper and lower regions, the grid spacing is 0.1 km and 0.3 km respectively, with a total of approximately 6.84×10^7 grids. To ensure the stability of the numerical simulation, five grids were used in one wavelength under the condition of a fourth-order precision. At the same time, the simulated low frequency was appropriately extended to a high frequency, and the upper limit of the frequency for the velocity pulses simulation was taken as 1.4 Hz. The detailed calculation parameters are listed in Table 3.

Results and discussion

Waveform comparison

The simulated and observed waveforms of the 28 velocity pulse histories of the near-field ground motions are shown in Fig. 7. The red dashed lines indicate the simulated results, the black solid lines indicate the observed records, and all the data are low-pass filtered with a cut-off frequency of 1.4 Hz. Most velocity histories match well regarding the amplitude and phase, and fewer pulses are recorded on the fault-parallel (FP) component (displaying complex
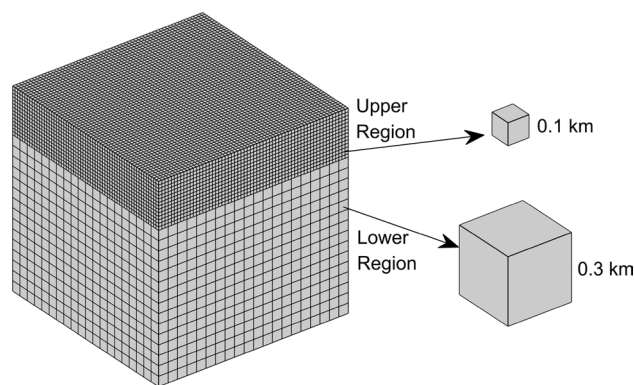
velocity pulses, the viscoelastic effect of the crustal medium needs to be considered. When the S-wave velocity is less than 1–2 km/s, the ratio of the attenuation factor Q to V_s is close to 0.02, and when the S-wave velocity is greater than 2 km/s, the ratio in the Los Angeles area is approximately 0.1 (Olsen et al. 2003). We set the viscoelastic properties of the velocity model according to existing studies in the region (Magistrale et al. 1992; Olson et al. 1984, 2003). The adopted velocity model is presented in Table 2.

The crust in the Northridge area is divided into grids with an interface of 8 km beneath the surface because the shallow strata in the region have smaller seismic velocities than the deep strata. The entire region is divided into small grids, considerable amounts of computational time and memory will be consumed. However, the region is divided into large grids, and the simulation results may numerically diverge. To satisfy the accuracy and efficiency of calculation at the

Fig. 6 Schematic diagram of 3D non-uniform grid configuration for the local region

Table 2 Relevant velocity structure model for the Northridge area

Depth (km)	Thickness (km)	V_p (km/s)	V_s (km/s)	Density (kg/m³)	Q
0	0.5	2.1	1.08	2100	22
0.5	3.5	4.0	2.15	2500	215
4.0	2.5	4.8	2.65	2600	265
6.5	14.0	6.1	3.50	2900	350
20.5	14.5	7.0	4.00	3000	400
35.0	∞	7.8	4.50	3300	450

Table 3 Calculation parameters used in this study

Model size (nx×ny×nz)	88.2×92.4×35
Total time steps	4000
Time step (s)	0.005
Upper limit frequency (Hz)	1.4
Total grid points	$6.84×10^7$
Receiving stations	53
Simulation area range	33.9° N–34.7° N, 118° W–119° W

waveforms) than on the fault-normal (FN) component (displaying simple waveforms). At the rupture front-end station NWP, the velocity waveforms exhibit one-side long-period velocity pulses, the pulse peak of the fault-normal component is greater than 100 cm/s, and the pulse period is approximately 2 s, while at the rupture back-end station PKC, the pulse peak and period of are approximately half of those at station NWP, and the fault-parallel component did not record the velocity pulse history. The velocity pulse is affected by the seismic Doppler effect and the orientation of the station, the energy of the rupture radiation of each sub-fault is stacked at the front end of the rupture, while the time it takes for the energy to reach the back end of the rupture is delayed; thus, the velocity histories of stations NWP and PKC are characterized by forward directivity and backward directivity effects, respectively.

Among the 7 stations on the hanging wall, station LAS is the farthest (8.44 km) from the fault plane; at this station, the pulse peaks of the two components are the smallest and basically equivalent, and the fault-parallel component has a more obvious two-side pulse than the fault-normal component in the velocity histories, which indicates that the fling-step effect has a greater influence on the vicinity of station LAS than does the directivity effect. Mavroeidis and Papageorgiou (2003) argued that the peak of the near-field pulse does not increase indefinitely, but there is a typical threshold of approximately 100 cm/s. In the actual recordings, the pulse peaks of the fault-normal component for stations RRS and SCW are approximately 120 cm/s. Compared with the fault-parallel components, the fault-normal components for stations RRS and LAD have larger peaks and smaller pulse periods, and the velocity pulses are also more significant. These differences are related to the positions of the stations on the active hanging wall and are greatly affected by the fling-step effect caused by the thrust motion along the fault. Stations SCE, SCW, JFA, and JFG are located at similar positions, but the actual recorded pulses are different, which is related to the local site of each station. For example, stations SCE and SCW are located on rock and soil, respectively; thus, the velocity history of SCW records a larger pulse peak than that of SCE, reflecting the amplification effect of the soil layer on the pulse peak.

On the footwall, the three stations (PDU, PDD, and SOV) near the initial rupture end of the fault are closer to asperity

Fig. 7 Comparison of the simulated (red dashed lines) and observed (black solid lines) waveform for the 28 velocity pulses. The station abbreviation along with the component name is shown above each curve. The maximum amplitudes in cm/s are shown to the right of the curves, simulated value is indicated above the end of each curve, and observed value is indicated below the end of each curve. The strong ground motion data applied low-pass filtering at 1.4 Hz
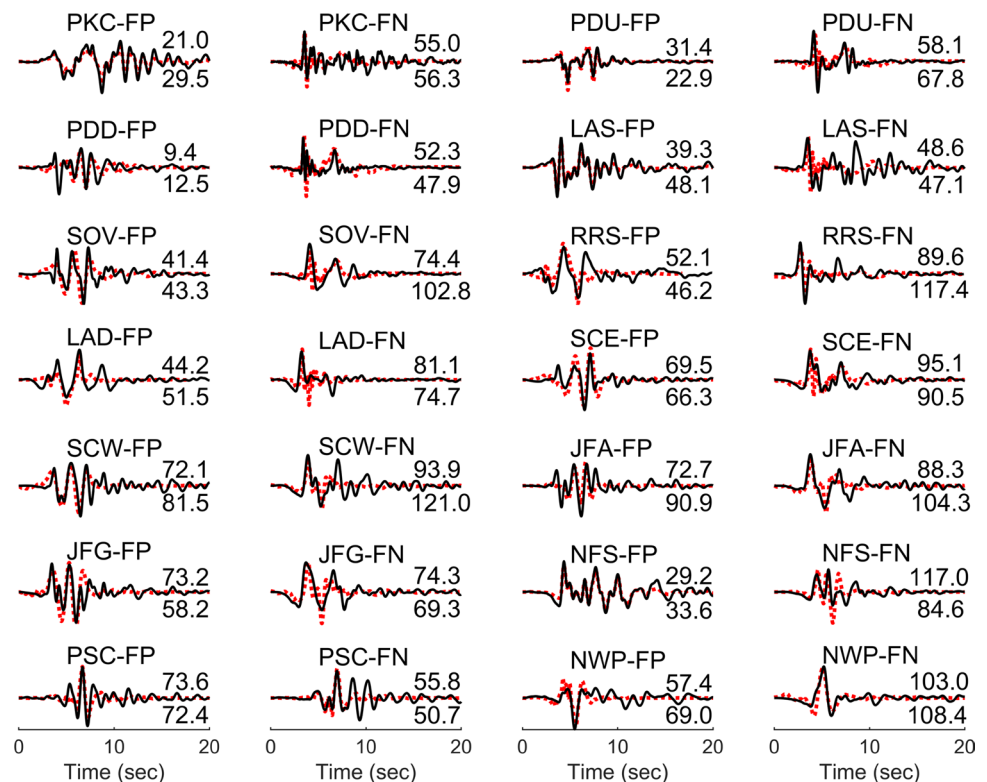
A than the two stations (NFS and PSC) near the front end of the rupture, and the former three stations exhibit more pronounced velocity pulses than the latter two, while the high amplitudes after the pulses on their velocity histories are mainly affected by the asperity B. Station SOV is the closest (5.3 km) to the fault plane with a recorded pulse peak greater than 100 cm/s on the fault-normal component, and the waveform has a large wave period after the initial pulse, which is related to the inhomogeneous distribution of the rise time on the fault plane. The small rise times of the nucleation zone produce short-period and high-amplitude velocity pulses, while the large rise times on the fault plane produce long-period and low-amplitude waveforms.

In the numerical simulation of velocity pulses, we found that the transverse component of the S-wave is larger than the radial component of the P wave due to the radiation of the ruptures on the subfaults, and thus, the fault-normal component has a larger pulse than the fault-parallel component at most near-field stations. Comparing the pulse peaks between the hanging wall and footwall stations, there are three velocity pulses (RRS-FN, SCW-FN, and JFA-FN) that exceed 100 cm/s on the hanging wall, while only SOV-FN recorded a velocity pulse of approximately 100 cm/s on the footwall. At the same time, station SCW on the hanging wall displays a larger pulse peak than station SOV on the footwall at a similar distance from the fault. Therefore, the stations on the active hanging wall are more affected by the asperities on the fault plane and more easily record the velocity pulses. It can be seen from the simulation results of all the stations that recorded the velocity pulses of the Northridge earthquake that the 3D finite difference method can effectively simulate long-period velocity pulses, but some of the short-period velocity waveforms are not ideal. A large amount of data was recorded throughout the near-field region of the Northridge earthquake, but the distribution of strong motion stations with pulse records was unbalanced, and the number of stations near the front end of the rupture was much smaller than that near the back end. It is therefore necessary to analyse the characteristics of the velocity pulses from the spatial distribution of near-field ground motions.

PGV analysis

The peak ground velocity (PGV) is one of the most important parameters reflecting the intensity of ground motion. It can provide a good reference for estimating the seismic intensity, determining seismic zoning, and future urban planning. The damage attributable to near-field strong motion is mainly related to long-period components, and the peak velocity is more likely than the peak acceleration to reflect the long-period characteristics of near-field ground motions (Wald et al. 1999; Xu and Xie 2005).

To analyse the distribution characteristics of the long-period PGV in the near-field region, we plot contour maps with an interval of 10 cm/s by using the simulated peaks from 53 stations (no pulses were recorded at 39 stations) and perform low-pass filtering with a cut-off frequency of 1.4 Hz for all the data; the simulated long-period PGV distribution is then compared with the actually observed records, as shown in Fig. 8. The simulated PGV is similar to the observed PGV with distribution characteristics along the fault strike. The PGV at the front end of the fault rupture has a wider distribution than that at the back end of the rupture, the former exhibits slower decay, and the near-field ground motion reflects the typical directivity effect. The peak ground velocities are similar between the horizontal components, but the intensity and attenuation of each component are different. The PGV on the fault-parallel component is significantly smaller than that on the fault-normal component, and velocity pulses are recorded more frequently on the fault-normal component. It can be seen from the spacing and intensity of the contours that the PGV decays faster in the vicinity of the fault, the decay rate of the PGV gradually decreases as the fault distance increases, and the fault-parallel component decays slower than the fault-normal component.

Strong ground motions are mainly concentrated in the vicinity of stations SCW and NWP, and the maximum peaks on the fault-parallel and fault-normal components are approximately 90 cm/s and 120 cm/s, respectively. The simulated value of the near-field long-period PGV is slightly smaller than the observed value in the local area. The reasons for this difference may include the uncertainties in the source parameters, the seismic wave disturbances caused by changes in the terrain, and the amplification of the ground motions in the Los Angeles Basin and San Fernando Basin.

Pseudo-velocity response spectra comparison

The pseudo-velocity response spectrum is presented as the maximum pseudo-velocity response curve of a single-degree-of-freedom elastic system that changes with the natural vibration period under a given ground motion. The response spectrum derives from the combination of structural dynamic characteristics (the natural vibration period, vibration mode, and damping) and ground motion; accordingly, the resonance effect of a structure in an earthquake can be calculated by the response spectrum. The characteristic period discussed in this paper refers to the period corresponding to the maximum amplitude of the pseudo-velocity response spectrum; the near-field velocity pulse of the Northridge earthquake has a large characteristic period, resulting in serious damage to long-period large-scale structures, especially lifeline engineering and building structures in the near-field region. Therefore, the characteristic period
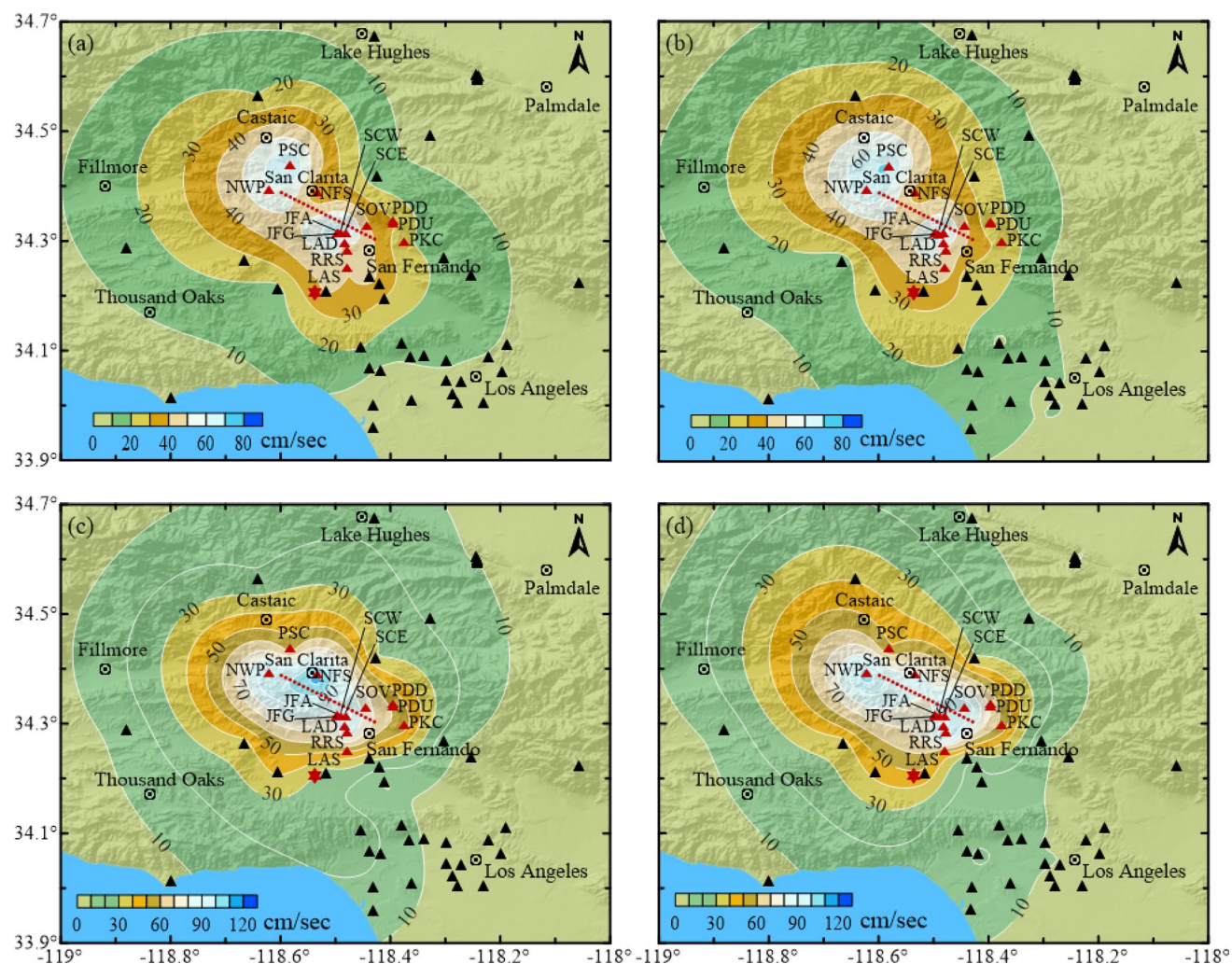
Fig. 8 Contour maps of PGV in cm/s obtained from 53 stations surrounding the fault. All the data are low-pass filtered by a frequency of 1.4 Hz. **a** Simulated values of the fault-parallel components; **b** observed values of the fault-parallel components; **c** simulated values of the fault-normal components; **d** Observed values of the fault-normal components

of the pseudo-velocity response spectrum is of great significance for engineering research.

The pseudo-velocity response spectra for the horizontal components of each station that recorded velocity pulses during the Northridge earthquake are shown in Fig. 9. The damping ratio is 5%, the period is 1–10 s, the red dashed line indicates the simulated response spectrum, and the black solid line indicates the observed response spectrum. There are some differences among the characteristic periods of the pseudo-velocity response spectra. For example, the characteristic period of the response spectrum of stations SOV, SCW, and NWP is approximately 2 s, and the characteristic period of stations PDU, LAS, and PSC is approximately 1 s, while the characteristic periods of stations RRS, LAD, and JFA on different components differ by approximately 1 s. Comparing the pseudo-velocity response spectra with the velocity histories, it can be determined that the characteristic

period of the response spectrum is positively correlated with the pulse period of the velocity history. The maximum spectral value of the pseudo-velocity response spectrum also shows some differences between the different components of each station. For example, the maximum spectral values of station NWP on the fault-parallel and fault-normal components are approximately 130 cm/s and 200 cm/s, respectively. Therefore, the maximum spectral value of the pseudo-velocity response spectrum is related to the pulse peak of the velocity history. From the overall comparison of the pseudo-velocity response spectra, it can be seen that the simulated values are close to the observed values; however, the simulated and observed spectra of stations PDU and PDD on the fault-normal component display some differences after the characteristic period, which is more likely to be affected by local site effects compared with the long-period surface waves.

Fig. 9 Comparison of the simulated (red dashed lines) and observed (black solid lines) pseudo-velocity response spectrum for the 28 pulses. The damping value is 5%
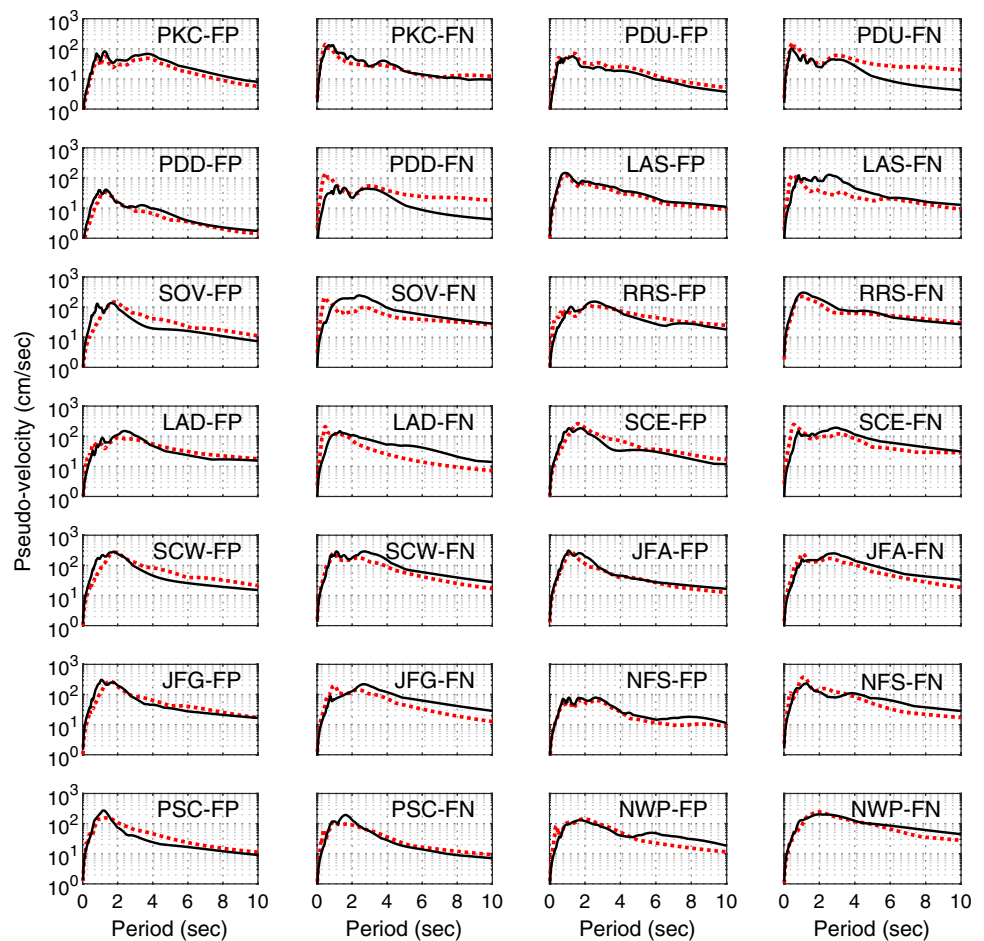
Arias intensity analysis

The distribution characteristics of the Arias intensity in the near-field region of the Northridge earthquake are shown in Fig. 10. The intensity decays with increasing fault distance, and the intensity in the vicinity of the fault decays faster than that in the region far from the fault; moreover, the area of the Arias intensity at the front end of the fault rupture is wider than that at the back end, and the Arias intensity on the fault-parallel component is smaller than that on the fault-normal component. There are some differences in the concentrated areas of large intensity values around the fault. Large values are concentrated around stations PSC and SCW on the fault-parallel component and around stations NFS, RRS, and PDU on the fault-normal component; these large value areas are also indicative of large earthquake disasters. The simulated values of the Arias intensity are basically consistent with the observed values, but there are differences in some local areas far from the fault, which may be related to the whole earthquake procedure, as well as changes in the topography and local site conditions.

Regression analysis

To verify the numerical simulation results of the near-field velocity pulses by the 3D finite difference method, regression analysis is performed on the simulated and observed values based on the least-squares method. The PGV and regression results for the horizontal components of 53 stations in the near-field region are shown in Fig. 11. The simulated values are similar to the observed values, and the PGV of each component exhibits a different attenuation trend with decreasing distance to the fault. The PGV on the fault-parallel component is smaller than that on the fault-normal component. The attenuation of the fault-parallel component occurs more slowly (i.e. the absolute slope of the regression line is small) within 18 km from the fault, but the attenuation of the two components occurs at a similar rate at distances greater than 18 km from the fault, which is basically consistent with the distribution characteristics of the PGV contours. One of the criteria for a velocity pulse that must be satisfied is a PGV greater than 30 cm/s. The velocity pulses on the fault-parallel and fault-normal components are most likely to be within 13 km and 15 km, respectively, of the fault, which
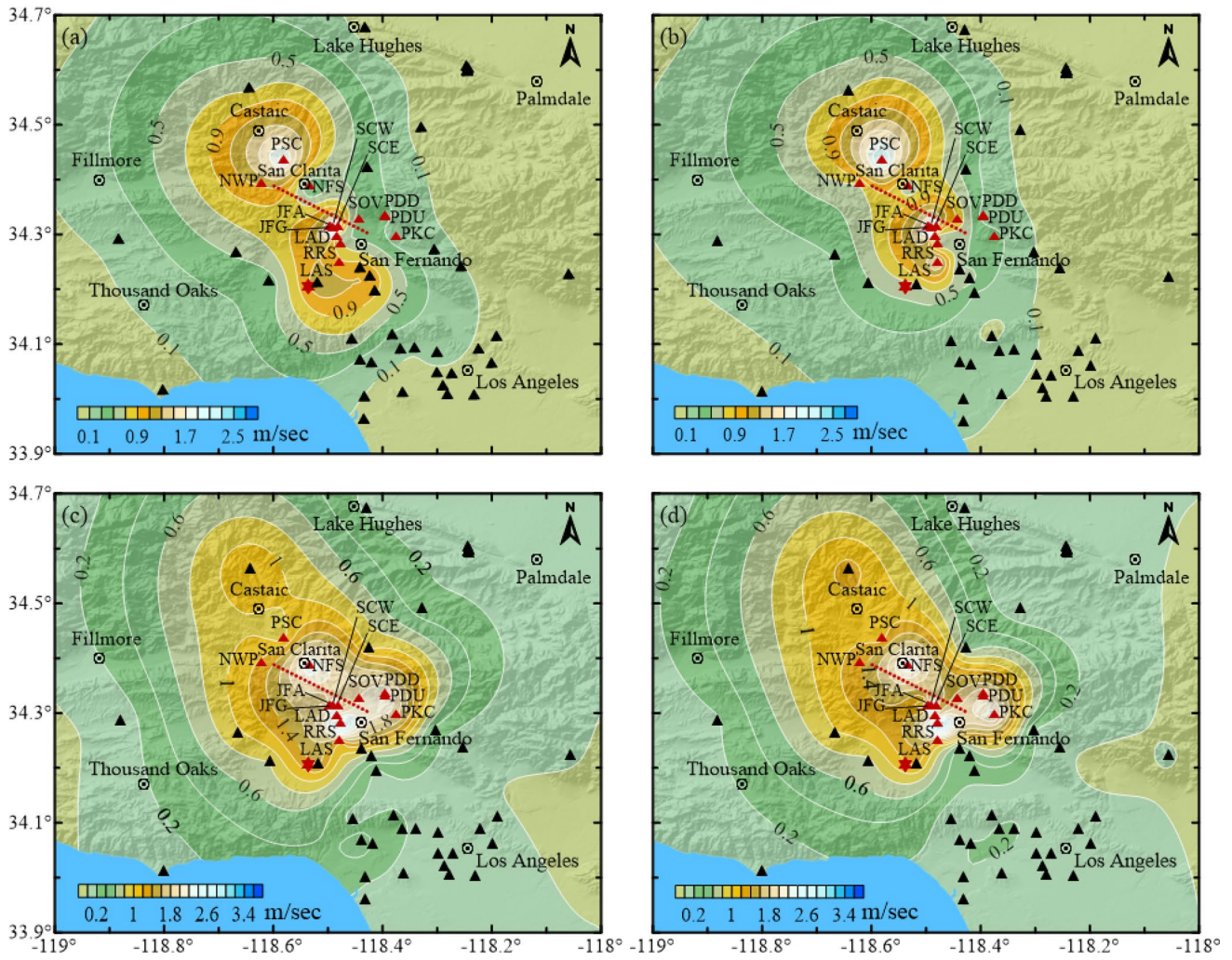
Fig. 10 Arias intensity in m/s distribution obtained from 53 stations surrounding the fault. **a** Simulated values of the fault-parallel components; **b** observed values of the fault-parallel components; **c** simu-lated values of the fault-normal components; **d** observed values of the fault-normal components
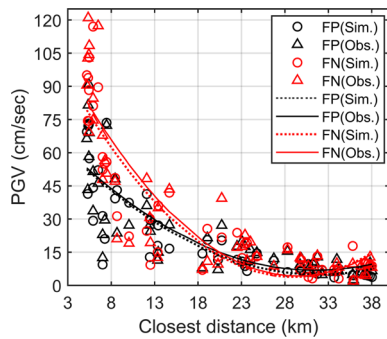

Fig. 11 Variations of PGV with the closest distance to fault plane for 53 strong ground stations. The simulated and observed values of the fault-parallel components are represented by black open circles and black open triangles, respectively. The simulated and observed values of the fault-normal components are represented by red open circles and red open triangles, respectively. The comparison of the regressions is represented by lines, where the simulated and observed values are indicated by the dashed and solid lines, respectively

also suggests that the source radiation effect produces large amplitudes along the direction perpendicular to the fault.

The characteristic period of the pseudo-velocity response spectrum is basically in the range of 1–2 s, and the spectral values corresponding to the vibration periods of 1, 1.5, and 2 s are taken from the response spectra. The simulated and observed values are also regressed, as shown in Fig. 12. It can be seen that the simulated results agree well with the observed records; the spectral values on the fault-normal component are larger than those on the fault-parallel component, and the attenuation of the former occurs more slowly than that of the latter, so the near-field velocity pulses are most likely to cause damage to structures along the direction perpendicular to the fault. In the seismic design of building structures, not only the short-period ground motions excited by active faults but also the long-period pulse-like ground motions should be considered. Clearly, the study of
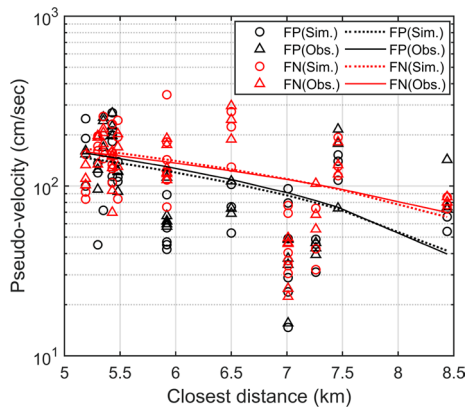
Fig. 12 Comparison of pseudo-velocity regression with the closest distance to fault plane for the 28 pulses

near-field velocity pulses is of great significance for earthquake prevention and disaster reduction.

Conclusions

The near-field long-period velocity pulses of the Northridge earthquake were simulated by the 3D finite difference method. The simulated velocity histories, PGV distribution, pseudo-velocity response spectra, and Arias intensities were compared with the real observed values, and regression analysis verified the feasibility of simulating the near-field velocity pulses by this method. The simulation results are expected to apply to near-field pulse-like ground motion assessments, seismic hazard analysis, and the study of nonlinear structural responses. The following conclusions can be drawn:

1. The source model affects the characteristics of the near-field long-period velocity pulses and the distribution of pulse-like ground motions. The rectangular asperity provides an important contribution to the pulse peaks, and the irregular asperity mainly affects the waveforms after the velocity pulses. One-side pulses on the fault-normal component are mainly affected by thrust slip and two-side pulses on the fault-parallel component affected by rupture direction. The velocity pulses on the fault-normal component are more abundant than those on the fault-parallel component; besides, the pulse period is positively correlated with the rise time, and the pulse peak is regulated by the seismic moment, the amount of slip, and the rise times on the subfaults. Some peaks exceed 100 cm/s.
2. The PGV contours exhibit an asymmetrical distribution in the near-field region, and the distribution at the front end of the rupture is larger than that at the back end.

The PGV exhibits irregular elliptical attenuation, and the PGV decay rate gradually decreases with increasing distance from the fault. Similar to the PGV distribution, the Arias intensity also exhibits a significant directivity effect and attenuation trend; the fault-normal component is larger than that on the fault-parallel component; and the intensity on the former decays faster than that on the latter, while the distributions of the maximum values on different components do not necessarily coincide.

3. The characteristic period of the pseudo-velocity response spectrum is basically in the range of 1–2 s, and the characteristic period is related to the pulse period. Velocity pulses greater than 30 cm/s are most likely to be distributed within approximately 15 km of the fault; in addition, the fault-normal component has a larger distribution range than the fault-parallel component. Hence, the near-field region should be considered an important area during the seismic design of building structures.

References

Aki K (1968) Seismic displacements near a fault. J Geophys Res 73(16):5359–5376

Aki K (1984) Asperities, barriers, characteristic earthquakes and strong motion prediction. J Geophys Res Solid Earth 89(B7):5867–5872

Aoi S, Fujiwara H (1999) 3D finite difference method using discontinuous grids. Bull Seismol Soc Am 89(4):918–930

Aoi S, Maeda T, Nishizawa N, Aoki T (2012) Large-scale ground motion simulation using GPGPU. AGU, fall meeting, S53G-06

Baker JW (2007) Quantitative classification of near-fault ground motions using wavelet analysis. Bull Seismol Soc Am 97(5):1486–1501

Beresnev IA, Atkinson GM (1998a) FINSIM-a FORTRAN program for simulating stochastic acceleration time histories from finite-faults. Seismol Res Lett 69(1):27–32

Beresnev IA, Atkinson GM (1998b) Stochastic finite-fault modeling of ground motions from the 1994 Northridge, California, earthquake. I. Validation on rock sites. Bull Seismol Soc Am 88(6):1392–1401

Bertero VV, Mahin SA, Herrera RA (1978) Aseismic design implications of near-fault San Fernando earthquake records. Earthq Eng Struct D 6(1):31–42

Boore DM (2003) Simulation of ground motion using the stochastic method. Pure Appl Geophys 160(3–4):635–676

Choudhury P, Chopra S, Roy KS, Sharma J (2016) Ground motion modelling in the Gujarat region of Western India using empirical Green's function approach. Tectonophysics 675:7–22

Dickinson BW, Gavin HP (2011) Parametric statistical generalization of uniform-hazard earthquake ground motions. J Struct Eng 137(3):410–422

Field EH, Zeng Y, Johnson PA, Beresnev IA (1998) Nonlinear sediment response during the 1994 Northridge earthquake: observations and finite source simulations. J Geophys Res Solid Earth 103(B11):26869–26883

Furumura T, Maeda T, Oba A (2019) Early forecast of long-period ground motions via data assimilation of observed ground motions and wave propagation simulations. Geophys Res Lett 46(1):138–147

Gao MT, Yu YX, Zhang XM, Wu J, Hu P, Ding YH (2002) Three-dimensional finite-difference simulations of ground motions in the Beijing area. Earthq Res Chin 18(4):356–364 (in Chinese)

Graves RW (1998) Three-dimensional finite-difference modeling of the San Andreas fault: source parameterization and ground-motion levels. Bull Seismol Soc Am 88(4):881–897

Hartzell S, Liu P, Mendoza C (1996) The 1994 Northridge, California, earthquake: investigation of rupture velocity, risetime, and high-frequency radiation. J Geophys Res Solid Earth 101(B9):20091–20108

Heaton TH, Hall JF, Wald DJ, Halling MW (1995) Response of high-rise and base-isolated buildings to a hypothetical Mw 7.0 blind thrust earthquake. Science 267(5195):206–211

Irikura K (1983) Semi-empirical estimation of strong ground motions during large earthquakes. Bull Disaster Prev Res Inst Kyoto Univ Jpn 33(2):63–104

Irikura K, Miyake H (2011) Recipe for predicting strong ground motion from crustal earthquake scenarios. Pure Appl Geophys 168(1–2):85–104

Iwaki A, Maeda T, Morikawa N, Miyake H, Fujiwara H (2016) Validation of the recipe for broadband ground-motion simulations of Japanese crustal earthquakes. Bull Seismol Soc Am 106(5):2214–2232

Ji C, Wald DJ, Helmberger DV (2002) Source description of the 1999 Hector Mine, California, earthquake, part I: wavelet domain inversion theory and resolution analysis. Bull Seismol Soc Am 92(4):1192–1207

Kamae K, Irikura K (1998) Source model of the 1995 Hyogo-ken Nanbu earthquake and simulation of near-source ground motion. Bull Seismol Soc Am 88(2):400–412

Kawase H, Aki K (1990) Topography effect at the critical SV-wave incidence: possible explanation of damage pattern by the Whittier Narrows, California, earthquake of 1 October 1987. Bull Seismol Soc Am 80(1):1–22

Kramer S (1996) Geotechical earthquake engineering. Prentice Hall, Upper Saddle River, NJ, pp 50–300

Li XX (2016) Study on extraction of the velocity pulse and effects of inclusion on ground motion. Institute of Engineering Mechanics, China Earthquake Administration, Beijing, pp 10–11 (in Chinese)

Li Z, Chen X, Gao M, Jiang H, Li T (2017) Simulating and analyzing engineering parameters of Kyushu earthquake, Japan, 1997, by empirical Green function method. J Seismol 21(2):367–384

Li Z, Gao M, Jiang H, Chen X, Li T, Zhao X (2018) Sensitivity analysis study of the source parameter uncertainty factors for predicting near-field strong ground motion. Acta Geophys 66(4):523–540

Liu T, Luan Y, Zhong W (2012) A numerical approach for modeling near-fault ground motion and its application in the 1994 Northridge earthquake. Soil Dyn Earthq Eng 34(1):52–61

Liu J, Zhang J, Sun Y, Zhao T (2016) Comparison of methods for seismic wavelet estimation. Prog Geophys 31(2):0723–0731 (in Chinese)

Li A, Liu Y, Dai F, Liu K, Wei M (2020) Continuum analysis of the structurally controlled displacements for large-scale underground caverns in bedded rock masses. Tunn Undergr Space Technol 97:103288

Luo Q, Chen X, Gao M, Li Z, Zhang Z, Zhou D (2019) Simulating the near-fault large velocity pulses of the Chi-Chi (M_W 7.6) earthquake with kinematic model. J Seismol 23(1):25–38

Maeda T, Morikawa N, Iwaki A, Aoi S, Fujiwara H (2014) Simulation-based hazard assessment for long-period ground motions of the Nankai Trough megathrust earthquake. AGU, fall meeting, S31C-4438

Maeda T, Iwaki A, Morikawa N, Aoi S, Fujiwara H (2016) Seismic-hazard analysis of long-period ground motion of megathrust earthquakes in the Nankai trough based on 3D finite-difference simulation. Seismol Res Lett 87(6):1265–1273

Magistrale H, Kanamori H, Jones C (1992) Forward and inverse three-dimensional P wave velocity models of the southern California crust. J Geophys Res Solid Earth 97(B10):14115–14135

Malhotra PK (1999) Response of buildings to near-field pulse-like ground motions. Earthq Eng Struct D 28(11):1309–1326

Mavroeidis GP, Papageorgiou AS (2003) A mathematical representation of near-fault ground motions. Bull Seismol Soc Am 93(3):1099–1131

Mikumo T, Hirahara K, Miyatake T (1987) Dynamical fault rupture processes in heterogeneous media. Tectonophysics 144(1):19–36

Mori J, Wald DJ, Wesson RL (1995) Overlapping fault planes of the 1971 San Fernando and 1994 Northridge, California earthquakes. Geophys Res Lett 22(9):1033–1036

Motazedian D, Atkinson GM (2005) Stochastic finite-fault modeling based on a dynamic corner frequency. Bull Seismol Soc Am 95(3):995–1010

Murotani S, Miyake H, Koketsu K (2008) Scaling of characterized slip models for plate-boundary earthquakes. Earth Planets Space 60(9):987–991

Oglesby DD, Archuleta RJ (1997) A faulting model for the 1992 Petrolia earthquake: can extreme ground acceleration be a source effect? J Geophys Res Solid Earth 102(B6):11877–11897

Olsen KB, Day SM, Bradley CR (2003) Estimation of Q for long-period (> 2 sec) waves in the Los Angeles basin. Bull Seismol Soc Am 93(2):627–638

Olson AH, Orcutt JA, Frazier GA (1984) The discrete wavenumber/finite element method for synthetic seismograms. Geophys J Int 77(2):421–460

Pitarka A (1999) 3D elastic finite-difference modeling of seismic motion using staggered grids with nonuniform spacing. Bull Seismol Soc Am 89(1):54–68

Pu WC, Liang RJ, Dai FY, Huang B (2017) An analytical model for approximating pulse-like near-fault ground motions. J Vib Shock 36(4):208–213 (in Chinese)

Ricker N (1943) Further developments in the wavelet theory of seismogram structure. Bull Seismol Soc Am 33(3):197–228

Somerville P, Irikura K, Graves R, Sawada S, Wald D, Abrahamson N, Iwasaki Y, Kagawa T, Smith N, Kowada N (1999) Characterizing crustal earthquake slip models for the prediction of strong ground motion. Seismol Res Lett 70(1):59–80

Wald DJ, Heaton TH, Hudnut KW (1996) The slip history of the 1994 Northridge, California, earthquake determined from strong-motion, teleseismic, GPS, and leveling data. Bull Seismol Soc Am 86(1B):S49–S70

Wald DJ, Quitoriano V, Heaton TH, Kanamori H (1999) Relationships between peak ground acceleration, peak ground velocity, and modified Mercalli intensity in California. Earthq Spectra 15(3):557–564

Wang Y (2015) The Ricker wavelet and the Lambert W function. Geophys J Int 200(1):111–115

Xu LJ, Xie LL (2005) Characteristics of frequency content of near-fault ground motions during the Chi–Chi earthquake. Acta Seismol Sin 18(6):707–716 **(in Chinese)**

Zeng Y, Anderson JG (1996) A composite source model of the 1994 Northridge earthquake using genetic algorithms. Bull Seismol Soc Am 86(1B):S71–S83

Zhang WB, Yu XW (2010) Strong ground motion simulation of the 1999 Chi–Chi, Taiwan, earthquake. J Earthq Eng Eng Vib 30(3):1–11 **(in Chinese)**